arXiv:1410.5668v1 [astro-ph.GA] 17 Oct 2014

Hot Ammonia in the Center of the Seyfert 2 galaxy NGC 3079

Yusuke Miyamoto*, Naomasa Nakai, Masumichi Seta, Dragan Salak, Kenzaburo Hagiwara†, Makoto Nagai and Shun Ishii‡,

miya@mx.ibaraki.ac.jp, nakai@physics.px.tsukuba.ac.jp, seta@physics.px.tsukuba.ac.jp, salak.dragan.fm@u.tsukuba.ac.jp, k-hagiwara@wr.jp.nec.com, nagai.makoto.ge@u.tsukuba.ac.jp, sishii@ioa.s.u-tokyo.ac.jp

Division of Physics, Faculty of Pure and Applied Sciences, University of Tsukuba, 1-1-1 Ten-nodai, Tsukuba, Ibaraki 305-8571

and

Aya Yamauchi

a.yamauchi@nao.ac.jp

Mizusawa VLBI Observatory, National Astronomical Observatory of Japan, 2-12 Hoshigaoka, Mizusawa, Oshu, Iwate 023-0861

(Received ; accepted)

Abstract

We present the results of ammonia observations toward the center of NGC 3079. The $NH_3(J,K) = (1,1)$ and $(2,2)$ inversion lines were detected in absorption with the Tsukuba 32-m telescope, and the $NH_3(1,1)$ through $(6,6)$ lines with the VLA, although the profile of $NH_3(3,3)$ was in emission in contrast to the other transitions. The background continuum source, whose flux density was ~ 50 mJy, could not be resolved with the VLA beam of $\lesssim 0\farcs09 \times 0\farcs08$. All ammonia absorption lines have two distinct velocity components: one is at the systemic velocity and the other is blueshifted, and both components are aligned along the nuclear jets. For the systemic components, the relatively low temperature gas is extended more than the high temperature gas. The blueshifted $NH_3(3,3)$ emission can be regarded as ammonia masers associated with shocks by strong winds probably from newly formed massive stars or supernova explosions in dense clouds in the nuclear megamaser disk. Using para-$NH_3(1,1)$, $(2,2)$, $(4,4)$ and $(5,5)$ lines with VLA, we derived the rotational temperature $T_{\rm rot} = 120 \pm 12$ K and 157 ± 19 K for the systemic and blueshifted components, respectively. The total column densities of $NH_3(0,0)$–$(6,6)$, assuming $T_{\rm ex} \approx T_{\rm rot}$, were $(8.85 \pm 0.70) \times 10^{16}$ cm^{-2} and $(4.47 \pm 0.78) \times 10^{16}$ cm^{-2} for the systemic and blueshifted components, respectively. The fractional abundance of NH_3 relative to molecular hydrogen H_2 for the systemic and blueshifted was $[NH_3]/[H_2] = 1.3 \times 10^{-7}$

and 6.5×10^{-8}, respectively. We also found the $F = 4$–4 and $F = 5$–5 doublet lines of OH $^2\Pi_{3/2}$ $J = 9/2$ in absorption, which could be fitted by two velocity components, systemic and redshifted components. The rotational temperature of OH was estimated to be $T_{\rm rot,OH} \geq 175$ K, tracing hot gas associated with the interaction of the fast nuclear outflow with dense molecular material around the nucleus.

Key words: radio lines: galaxies — radio lines: ISM — galaxies: ISM — galaxies: individual (NGC 3079)

1. Introduction

Galactic winds influence galaxy evolution because they play an important role in the cycle of material transport in the galaxy. The winds are driven by supernovae and/or AGNs. One of the clearest examples of a superwind is the prominent bubble emerging from the nucleus (e.g., Duric et al. 1988) of the edge-on ($i = 84°$; Irwin & Seaquist 1991) disk galaxy NGC 3079 (figure 1) at a distance of 19.7 Mpc (Springob et al. 2009). NGC 3079 is classified as a LINER (Heckman 1980) or Seyfert 2 galaxy (Ford et al. 1986). Optical spectroscopy showed gas motions with high velocity across the lobes and unusually the high [N II]/H α line ratio which indicates the presence of shocks (Veilleux et al. 1994). Cecil et al. (2001) explained the morphology and kinematics of gas in NGC 3079 by a model of a starburst-driven wind. Yamagishi et al. (2010), however, reported a relatively low star formation rate of 2.6 $M_\odot\,{\rm yr}^{-1}$ for the central 4-kpc region of the galaxy from infrared observations with the AKARI satellite. Duric et al. (1988) proposed an alternative model in which an AGN-driven wind from the nucleus was directed toward the galaxy minor axis by interactions with dense gas surrounding the nucleus. The interactions cause shocks that explain the observed strength of H_2 $\nu = 1$–0 $S(1)$ emission by collisional excitation (Hawarden et al. 1995; Meaburn et al. 1998) and heat dust to a temperature of ~ 1000 K (Israel et al. 1998), although the contribution of the jets from the AGN to the Hα flux of the lobes is $\sim 10\%$ (Cecil et al. 2001).

Investigations of the physical properties of molecular gas around the nucleus are helpful to understand the nuclear power source of NGC 3079. The molecular gas is abundant in the central region (Sofue & Irwin 1992; Irwin & Sofue 1992; Sofue et al. 2001; Koda et al. 2002) and the dense gas concentrates toward the center (Kohno et al. 2001). The concentration can be explained by gas inflow toward the center as a result of the removal of the gas angular momentum with bar potential (e.g., Nishiyama et al. 2001), where the bar structure in NGC 3079

* Present Address: Center for Astronomy, Ibaraki University, 2-1-1 Bunkyo, Mito, Ibaraki 310-8512

† Present Address: NEC Aerospace Systems, Ltd., 1-10, Nissin-cho, Fuchu, Tokyo, 183-8501

‡ Present Address: Institute of Astronomy, School of Science, University of Tokyo, Osawa 2-21-1, Mitaka, Tokyo, 181-0015

Table 1. Parameters of NGC 3079

Parameter	Value	Reference
R.A. (J2000.0)	$10^{\rm h}01^{\rm m}57\overset{\rm s}{.}803$	1
Decl. (J2000.0)	$+55°40'47\overset{''}{.}24$	
Distance	19.7 Mpc	2
Morphological type	SB(s)c edge-on	3
Nuclear Activity	LINER / Seyfert 2	4, 5
Systemic Velocity (LSR)	1116 km s^{-1}	6

References. — (1) Petrov & Taylor 2011; (2) Springob et al. 2009; (3) de Vaucouleurs et al. 1991; (4) Heckman 1980; (5) Ford et al. 1986; (6) Irwin & Seaquist 1991

has been resolved clearly in the velocity domain (Koda et al. 2002).

Ammonia (NH_3) is a useful thermometer (e.g., Walmsley & Ungerechts 1983; Danby et al. 1988) for relatively dense molecular gas ($n_{\rm H_2} \sim 10^{3-4}$ cm^{-3}). NH_3 has a symmetrical top structure which shows inversion doublets caused by the nitrogen atom tunneling through the potential barrier at the plane of three hydrogen atoms. The allowed dipole transitions of NH_3 are $\Delta J = \pm 1$ and $\Delta K = 0$, because the dipole moment corresponds to the symmetry axis of the molecule. The non-metastable levels $[J, K(\neq J)]$ decay rapidly (Einstein A-coefficients $\sim 10^{-1}$ s^{-1}) via the far-infrared $\Delta J = 1$ transitions, and the radiative $\Delta K = \pm 3$ transitions are very slow ($A \sim 10^{-9}$ s^{-1}; Oka et al. 1971), hence the metastable $[J,K(=J)]$ levels ($A \sim 10^{-7}$ s^{-1}) are populated. The relative populations of the metastable levels are mainly determined by collisions and thus follow the Boltzmann distribution. The rotational temperature can be derived from the ratio of column densities of the metastable levels. The adjacent inversion lines in frequency (see subsection 2.1) allow us to measure the lines simultaneously with the same telescope and receiver and thus to evaluate the line ratios accurately owing to the similar beam sizes, same telescope pointing and atmospheric conditions.

In this paper we report the detections of NH_3 (plus highly excited OH) lines toward the center of NGC 3079. We derive their rotational temperatures and estimate the NH_3 column density and the abundance under high temperature. The basic parameters of NGC 3079 adopted in this paper are summarized in table 1. Velocities used here are in the radio definition and with respect to the local standard of rest (LSR).

2. Observations

2.1. Tsukuba 32-m

Observations of ammonia toward the center of NGC 3079 were made in March and April 2008 with the Tsukuba 32-m telescope of the Geospatial Information Authority of Japan. The

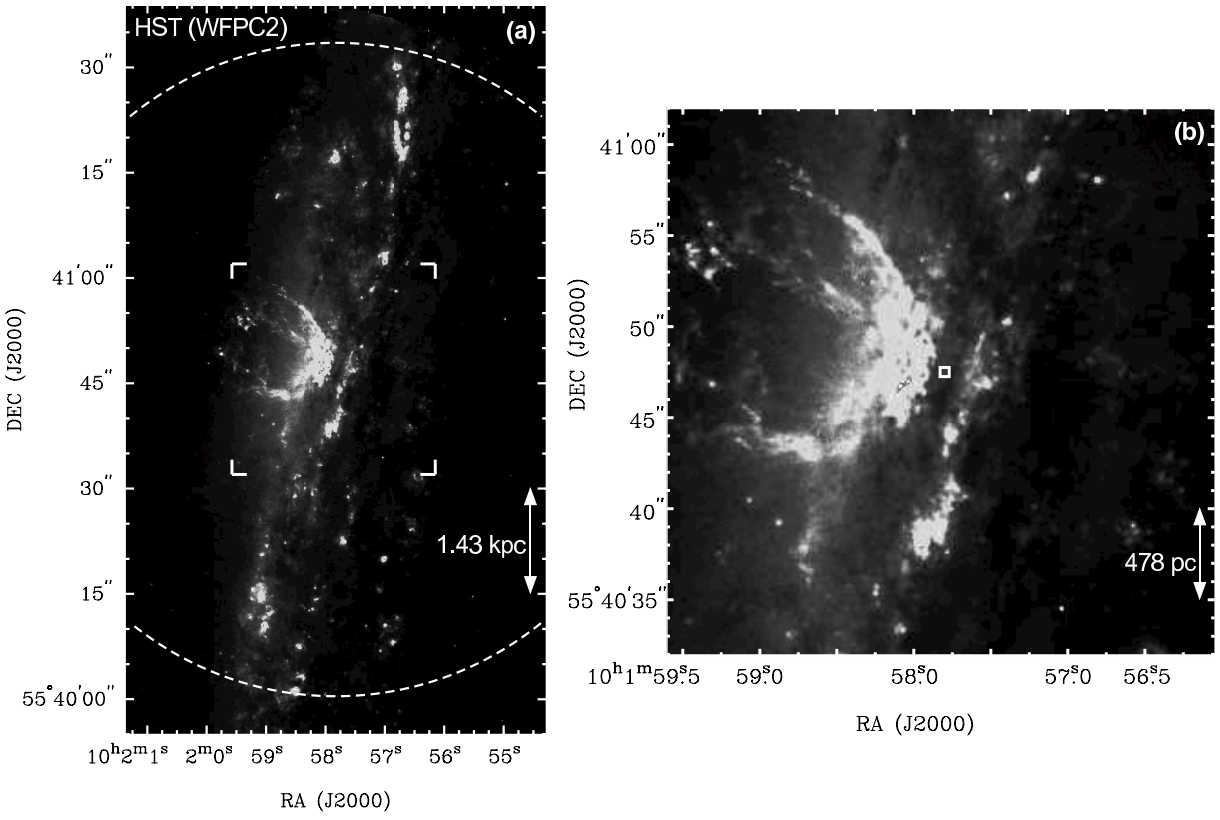

Fig. 1. Optical image of NGC 3079. (a) *HST* WFPC2 image of [N II] and H α line emissions, obtained from the HST data archive. The dashed lines represent the beam size of ammonia observations with the Tsukuba 32-m (*HPBW*= 93″.) (b) Enlargement of the central region in (a). The region marked by the solid box corresponds to the frame of figure 4.

full half-power beam width was HPBW= $93'' \pm 6''$ at 24 GHz, corresponding to 8.9 kpc at the distance of the galaxy (19.7 Mpc). The main beam efficiency of the antenna $\eta_{\rm mb}$ was measured, using Jupiter whose brightness temperature was adopted to be $T_{\rm b} = 138 \pm 7$ K at $\lambda = 1.3$ cm (de Pater et al. 2005), and depended on the elevation of the antenna with the maximum value of $\eta_{\rm mb} = 0.44 \pm 0.02$ at $EL = 38°$ at 24 GHz. The aperture efficiency was maximumly $\eta_{\rm a} = 0.37 \pm 0.01$ at $EL = 38°$, calculated from the main beam efficiency and the beam size, and confirmed by observing 3C 286. The sensitivity of the antenna was $S/T_{\rm A}^{*} = 9.28$ Jy K^{-1} at 24 GHz, where S is the flux density and $T_{\rm A}^{*}$ the antenna temperature.

The receiver front-end utilized a HEMT amplifier cooled to 11 K, equipped with a circular polarized feed. Its frequency coverage was 19.5–25.1 GHz. The receiver back-end was a 16384-channels FFT spectrometer. The total bandwidth and frequency resolution of the spectrometer were about 1.0 GHz and 55 kHz, which corresponded to 1.3×10^4 km s^{-1} and 0.69 km s^{-1} at 24 GHz, respectively. The bandwidth allowed us to observe four inversion transitions of ammonia, $(J,K) = (1,1)$–$(4,4)$, simultaneously (see table 2).

The line intensity was calibrated by the chopper wheel method, yielding an antenna

temperature, $T_{\rm A}^*$, corrected for both atmospheric and antenna ohmic losses (Ulich & Haas 1976). The typical system noise temperatures during the observations were 80-120 K (SSB) in $T_{\rm A}^*$ at observing elevations. The main beam brightness temperature, $T_{\rm mb}(\equiv T_{\rm A}^*/\eta_{\rm mb})$, was converted from $T_{\rm A}^*$ using the main beam efficiency of the antenna at each observing elevation. The observations were made by position-switching with an integration time of 10 s per scan. The telescope pointing was checked every 1 hr by observing H_2O maser of the Mira-type variable star R UMa, and the resultant pointing error was about $10''$–$20''$.

The spectral data were reduced with the NEWSTAR software which was developed at the Nobeyama Radio Observatory[1](NRO). The spectra were flagged and averaged after linear baseline subtraction, resulting in total observing time (ON source) was about 10.5 hours. All of the averaged spectra were bound up every 64 channels to reduce the noise level, resulting in a frequency resolution of 3.6 MHz or a velocity resolution of 45 km s^{-1} at 24 GHz.

2.2. VLA

Observations of ammonia in NGC 3079 were carried out with the A-configuration of the Karl G. Jansky Very Large Array (VLA) of the National Radio Astronomy Observatory[2](NRAO) of USA over a period from October 2012 through January 2013. The K-band receivers and the new WIDAR correlators were used for the dual-polarization. The correlator in each polarization was composed of 8 subbands whose bandwidth and frequency resolution were 128 MHz and 1 MHz, respectively, and thus the total bandwidth was 1024 MHz. The total bandwidth allowed us to observe $NH_3(J,K) = (1,1)$–$(3,3)$ simultaneously in the frequency band centered on 23.525 GHz and later $(J,K) = (4,4)$–$(6,6)$ centered on 24.590 GHz. The different UV coverages for the low and high frequency setting resulted in the different sizes of the synthesized beams (table 2). Observing time was 5 hrs for each frequency band, and totally 10 hrs. Antenna pointing was checked every 60 min by observing J0958+6533 with the X-band receiver, and the flux density at the K-band was calibrated by 3C 147. We tracked J0958+6533 every 2.5 min to calibrate time variations of amplitude and phase. The data were also used to determine the bandpass.

The observed data were processed using the Common Astronomy Software Applications (CASA; McMullin et al. 2007). The data obtained at different observing tracks were combined after subtracting continuum emission determined at the absorption-free channels and rearranging the velocity resolution to be 15 km s^{-1} and the velocity range to be 550–1750 km s^{-1}. To image the continuum emission, we used the flux density at the absorption-free channels. The imaging was performed with the CLEAN-algorithm in CASA. CLEAN maps were obtained

[1] The Nobeyama Radio Observatory is a branch of the National Astronomical observatory of Japan, National Institute of Natural Sciences.

[2] The National Radio Astronomy Observatory is a facility of the National Science Foundation operated under cooperative agreement by Associated Universities, Inc.

Table 2. Observational parameters with the VLA

Transitions	Frequency (GHz)	Beam Size (arcsec)*
$NH_3(2,1)$	23.098819	0.083×0.077
$NH_3(1,1)$	23.694506	0.083×0.077
$NH_3(2,2)$	23.722634	0.083×0.077
$NH_3(3,3)$	23.870130	0.083×0.077
$NH_3(4,4)$	24.139417	0.091×0.071
$NH_3(5,5)$	24.532989	0.089×0.069
$NH_3(6,6)$	25.056025	0.087×0.067
OH $^2\Pi_{2/3} J = 9/2$ $F = 4-4$	23.8176153	0.083×0.077
OH $^2\Pi_{2/3} J = 9/2$ $F = 5-5$	23.8266211	0.083×0.077

* $0\farcs08$ corresponds to 7.6 pc at the distance of NGC 3079.

considering the briggs weighting mode on the data with robust of 0.5. The resultant maps are 300×300 pixels with $0\farcs01$ per pixel. The synthesized beams are given in table 2.

3. Results

3.1. Tsukuba 32-m

Absorption lines of NH_3 $(J,K) = (1,1)$ and $(2,2)$ toward the center of NGC 3079 were detected with the Tsukuba 32-m telescope (figure 2). The two lines are so broad that they overlap each other for the rest frequency difference of 28.1 MHz corresponding to the velocity difference $\Delta V = 356$ km s^{-1}. To separate the spectrum into $NH_3(1,1)$ and $(2,2)$ components, we adopt a double Gaussian fitting function,

$$F(v) = T_{\rm mb,11} \exp \frac{-(v - V_{\rm LSR,11})^2}{2\sigma_{11}^2} + T_{\rm mb,22} \exp \frac{-(v - V_{\rm LSR,22} - \Delta V)^2}{2\sigma_{22}^2}, \quad (1)$$

where v is $V_{\rm LSR}$ in figure 2, $T_{\rm mb,11}$ and $T_{\rm mb,22}$ the main-beam brightness temperature, $V_{\rm LSR,11}$ and $V_{\rm LSR,22}$ the velocity relative to the local standard of rest (LSR), and σ_{11} and σ_{22} the velocity dispersion of $NH_3(1,1)$ and $(2,2)$, respectively. Figure 2 shows the result of least-square fitting of the function $F(v)$ to the observed spectrum, where the green, blue, and red lines show $NH_3(1,1)$, $(2,2)$, and the combination of them, respectively. Table 3 gives the fitting parameters of the main-beam brightness temperatures ($T_{\rm mb}$), the velocities ($V_{\rm LSR}$), and the full-width at half-maximum ($\Delta v_{1/2} = \sqrt{8 \ln 2}\sigma$). The velocities, $V_{\rm LSR} = 1113 \pm 83$ km s^{-1} for $NH_3(1,1)$ and 1122 ± 38 km s^{-1} for $NH_3(2,2)$ are consistent with the systemic velocity of the galaxy $V_{\rm sys} = 1116 \pm 1$ km s^{-1} (Irwin & Seaquist 1991), within the errors. $NH_3(3,3)$ line is undetected at the noise level of $\Delta T_{\rm mb} \sim 1.39$ mK as observations with the GBT (Mangum et al. 2013). In addition, the noise level of $\Delta T_{\rm mb} \sim 1.23$ mK is not low enough to detect an absorption

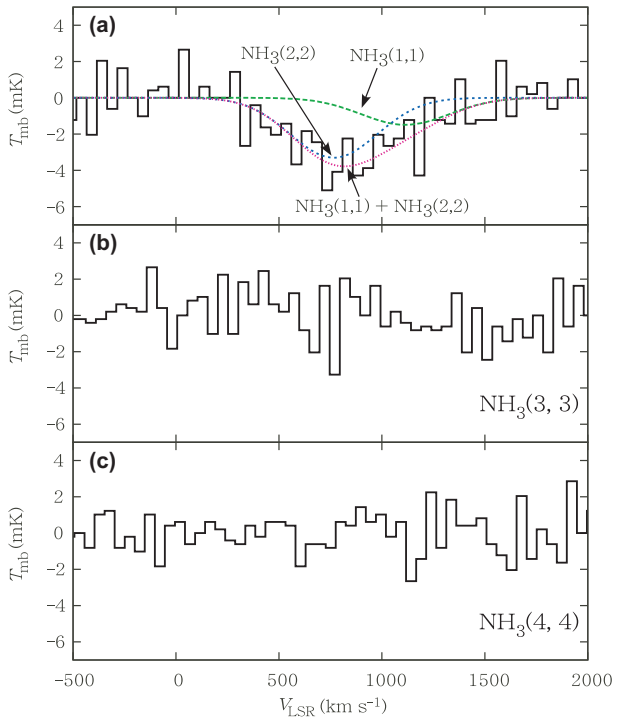

Fig. 2. Continuum-subtracted spectra of NH_3 toward the central region of NGC 3079 with the Tsukuba 32-m. The velocities $V_{\rm LSR}$ are with respect to the rest frequencies of $NH_3(1,1)$, $NH_3(3,3)$, and $NH_3(4,4)$ in figure (a), (b), and (c), respectively.

Table 3. The fitted parameters

Transitions	$T_{\rm mb}$ (mK)	$V_{\rm sys}$ (km s^{-1})	$\Delta v_{1/2}$ (km s^{-1})
$NH_3(1,1)$	-1.43 ± 0.45	1113 ± 83	504 ± 167
$NH_3(2,2)$	-3.31 ± 0.47	1122 ± 38	499 ± 75

line of $NH_3(4,4)$ whose intensity is expected to be comparable to that of $NH_3(1,1)$.

The peak flux densities for $NH_3(1,1)$ and $NH_3(2,2)$ are derived to be -5.7 ± 1.8 mJy and -13.2 ± 2.0 mJy, respectively, from the conversion of $S/T_{\rm A}^*$ in section 2.1. These flux densities are lower than those with the GBT (-18.5 mJy and -22.6 mJy for $NH_3(1,1)$ and $NH_3(2,2)$, respectively; Mangum et al. 2013). Since the beam sizes (HPBW $\approx 93''$) of the Tsukuba 32-m is larger than those (HPBW $\approx 30''$) of GBT, the difference may be caused (1) by the beam dilution of the absorption lines, and (2) by contamination from emission in the galactic disk because the molecular gas is extended over the radius of $r \sim 70''$ (Braine et al. 1997) while it is expected that the continuum source is over $r \sim 15''$ (e.g., Duric et al. 1988). We, however, should mention the possibility that the spectra for the Tsukuba 32-m are affected by instrumental and atmospheric instabilities that lead to poor spectral baselines and uncertain line profiles.

3.2. VLA

3.2.1. Continuum Emission

We detected an unresolved continuum source (contours in figure 4) with the resolution of $\leq 0\farcs09 \times 0\farcs08$ (beam size in table 2), corresponding to 8.6×7.6 pc, at R.A. (J2000.0)= $10^{\rm h}01^{\rm m}57\fs803$, Decl. (J2000.0)= $55°40'47\farcs25$, which was the same as the position measured with VLBI at 5 GHz, R.A. (J2000.0)= $10^{\rm h}01^{\rm m}57\fs8034$, Decl. (J2000.0)= $55°40'47\farcs243$ (Petrov & Taylor 2011). The measured flux density of about 50 mJy (table 4) is smaller than the value of ~ 80 mJy at $\lambda \sim 1.2$ cm expected from the flux density of 65 mJy at 4866 MHz and the spectrum index of $\alpha = +0.15$ (where $S_\nu \propto \nu^\alpha$) determined from the ratio of 1465 and 4866 MHz flux densities with the angular resolution of $\sim 1''$ (Duric et al. 1988), and than the value of 174 mJy at $\lambda \sim 1.2$ cm measured with the beam size of $\sim 30''$ by the GBT (Mangum et al. 2013). On the other hand, within a $0\farcs015$ radius from the center, some distinct continuum sources were identified with VLBI, and the total flux density was 38 ± 5 mJy at $\lambda \sim 1.3$ cm [components A, B, C and E in Yamauchi et al. (2004)]. Considering these results and the detectable largest angular scale of $\sim 2''$ by the VLA, it is indicated that there are continuum sources extended to more than $r \sim 1''$.

3.2.2. Ammonia Inversion Lines

Figure 3 shows the spectra measured with the VLA. The six ammonia inversion lines, $NH_3(1,1)$ to (6,6), are detected in absorption against the continuum source, although the profile of the $NH_3(3,3)$ line is anomalous. The spectra of $NH_3(1,1)$ and (2,2) do not overlap each other, rather clearly separate in velocity owing to narrower velocity widths, unlike the result of the 32-m (figure 2). This could be because VLA, with synthesized beam size $\approx 0\farcs08$ and detectable largest angular scale $\sim 2''$, observed much smaller regions than the 32-m (beam sizes $\approx 93''$) did and thus did not detect components broad in space and velocity (e.g., the rotation velocity of the galactic disk is $\sim$ 260–300 km s^{-1} at $r \gtrsim 1''$; Sofue et al. 2001). In figure 3, all the metastable NH_3 absorption lines show two distinct velocity components: one is at the systemic velocity ($V_{\rm LSR} \sim 1116$ km s^{-1}) and the other is blueshifted ($V_{\rm LSR} \sim 1020$ km s^{-1}). We fitted Gaussian profiles to the observed absorption lines. Table 4 gives the resultant parameters of the flux densities (S), the velocities ($V_{\rm LSR}$), and the optical depths (τ, see equation (2)) at the absorption peak, the line widths ($\Delta v_{1/2}$) and the optical depths integrated over the line profiles ($\int \tau dv$) for the systemic and blueshifted components.

Figure 4 shows the distribution of the intensities of the $NH_3(1,1)$, (2,2), (4,4), (5,5), and (6,6) lines integrated at $V_{\rm LSR} \approx$ 835–1180 km s^{-1}, including both the systemic and blueshifted components, and of the intensity of the $NH_3(3,3)$ absorption line integrated at $V_{\rm LSR}$ =1045–1165 km s^{-1}. The figure indicates that there is abundant molecular gas in front of the nuclear radio continuum source, although the distribution could not be resolved with the spatial resolution of $\lesssim 9$ pc (but see section 4.4 for more detail discussion).

The absolute flux densities of $NH_3(1,1)$–$(6,6)$ absorption lines except $NH_3(3,3)$ are

about half of those with the GBT whose beam size is HPBW $\approx 30''$ (Mangum et al. 2013). For the systemic components, the ratio of the flux densities with GBT to VLA decreases with the excitation level (table 5). This indicates that the relatively low temperature gas is more extended than the high temperature gas. In contrast, for the blueshifted components, the flux density ratio increases at the higher transitions of $NH_3(4,4)$ and $(5,5)$.

At the blueshifted velocity, the $NH_3(3,3)$ line shows a conspicuous spectrum which is not absorption but emission in contrast to the other NH_3 transition (figure 5). H(81)β and He(81)β recombination lines, whose frequencies are close to $NH_3(3,3)$ (table 6), may also explain the emission features. However, the emissions in the next transition, i.e., H(80)β and He(80)β, were not detected (figure 5). We therefore focus on $NH_3(3,3)$ maser as the most likely candidate of the emission features and discuss in more detail in subsection 4.1.

3.2.3. OH $^2\Pi_{2/3} J = 9/2$ Absorption Lines

We also found a wide absorption line with the width of $\Delta v_{1/2} \gtrsim 290$ km s^{-1} (figure 7) in the correlator subband which covered frequencies from 23.781 to 23.909 GHz, including the $NH_3(3,3)$ line. Considering the systemic velocity of NGC 3079 ($V_{\rm sys} = 1116$ km s^{-1}), the $F = 4$–4 and $F = 5$–5 doublet lines of OH $^2\Pi_{3/2}$ $J = 9/2$ and the HC_9N ($J = 41$–40) whose rest frequency of 23.8176153, 23.8266211 and 23.822265 GHz[3], respectively, are appropriate candidates for the absorption line. We, however, ruled out HC_9N ($J = 41$–40) because no absorption feature of the HC_9N ($J = 40$–39) transition (rest frequency, 23.241246 GHz) was confirmed in our VLA data. On the other hand, detections of the absorption lines at the ground state of OH $^2\Pi_{3/2} J = 3/2$ (rest frequencies, 1665- and 1667-MHz) toward the center of NGC 3079 have been reported (e.g., Hagiwara et al. 2004). So far the absorption lines at the $^2\Pi_{3/2}$ $J = 9/2$ state (excitation level of 511 K above the ground state, Walmsley et al. 1986) have been found toward some compact H II regions in the Galaxy (e.g., Winnberg et al. 1978; Baudry et al. 1981; Walmsley et al. 1986) and toward the center of Arp 220 (Ott et al. 2011). We therefore deduce that the absorption is caused by OH $^2\Pi_{3/2}$ $J = 9/2$ $F = 4$–4 and $F = 5$–5.

Figure 6 (right) shows the OH intensity map integrated at $V_{\rm LSR} = 790$–1375 km s^{-1} with respect to the rest frequency of OH $^2\Pi_{3/2}$ $J = 9/2$ $F = 4$–4. The structure cannot be resolved with the angular resolution of $0.''083 \times 0.''077$. The $F = 4$–4 and $F = 5$–5 doublet lines are spaced by 113 km s^{-1}, corresponding to the velocity separation between the dips in the wide spectrum, e.g., the components at $V_{\rm sys} \sim 1200$ km s^{-1} and ~ 1310 km s^{-1} in figure 7. Assuming that each doublet line has same velocity components, the wide absorption features can be fitted by two velocity components, $V_{\rm (OH,sys)} = 1085 \pm 4$ km s^{-1} and $V_{\rm (OH,red)} = 1302 \pm 2$ km s^{-1} (table 7). These velocity components are different from the velocities at the ground state of OH $^2\Pi_{3/2} J = 3/2$ (1011.9 ± 0.9 km s^{-1} and 1113.5 ± 2.0 km s^{-1}; Hagiwara et al. 2004) and NH_3, not showing the blueshifted components but the redshift. Although H I absorption toward the nucleus has

[3] F. J. Lovas et al., NIST Recommended Rest Frequencies for Observed Interstellar Molecular Microwave Transitions (http://physics.nist.gov/cgi-bin/micro/table5/start.pl).

Table 4. NH_3 parameters

Transitions	S^* (mJy)	$V_{\rm LSR}$ * (km s^{-1})	$\Delta v_{1/2}$ (km s^{-1})	τ^*	$\int \tau dv$ (km s^{-1})	$S_{\rm cont}$ (mJy)
NH_3	Systemic Components					
(1,1)	-8.15 ± 0.22	1117 ± 1	43 ± 1	0.176 ± 0.005	8.01 ± 0.35	50.62 ± 0.22
(2,2)	-10.28 ± 0.38	1117 ± 1	39 ± 2	0.227 ± 0.010	9.38 ± 0.59	50.62 ± 0.30
(3,3)	-1.23 ± 0.38	1133 ± 4	36 ± 7	0.025 ± 0.008	0.66 ± 0.30	49.99 ± 0.28
(4,4)	-9.18 ± 0.31	1116 ± 1	35 ± 1	0.194 ± 0.007	7.30 ± 0.41	52.08 ± 0.42
(5,5)	-7.34 ± 0.28	1116 ± 1	31 ± 2	0.158 ± 0.007	5.29 ± 0.34	50.10 ± 0.39
(6,6)	-10.00 ± 0.36	1117 ± 1	36 ± 2	0.228 ± 0.010	8.69 ± 0.54	49.09 ± 0.47
	Blueshifted Components					
(1,1)	-1.75 ± 0.18	1017 ± 3	65 ± 8	0.035 ± 0.004	2.43 ± 0.40	
(2,2)	-2.34 ± 0.27	1023 ± 5	84 ± 14	0.047 ± 0.006	4.25 ± 0.88	
(3,3)	1.54 ± 0.45	953 ± 16	165 ± 40	...	...	
(4,4)	-1.60 ± 0.20	1015 ± 6	95 ± 20	0.031 ± 0.004	3.14 ± 0.77	
(5,5)	-1.23 ± 0.15	1009 ± 10	122 ± 34	0.025 ± 0.003	3.23 ± 0.99	
(6,6)	-2.07 ± 0.24	1021 ± 5	87 ± 15	0.043 ± 0.005	4.00 ± 0.85	

* Values at the absorption peak after Gaussian fitting.

the redshifted component (Sawada-Satoh et al. 2001), the velocity of $V_{\rm LSR} = 1238 \pm 3$ km s^{-1} and the line width of $\Delta v_{1/2} = 32 \pm 6$ km s^{-1} are inconsistent with those of OH $^2\Pi_{3/2}$ $J = 9/2$. The highly excited OH line (energy level = 511 K) therefore traces hot gas with the anomalous dynamics in the central region, which may be associated with the hot dust ($T_{\rm d} \sim 1000$ K; Israel et al. 1998) heated by the interaction of the fast nuclear outflow with dense and dusty molecular material around the nucleus (e.g., Hawarden et al. 1995; Meaburn et al. 1998). In addition, the wide line widths in OH $^2\Pi_{3/2}$ $J = 9/2$ might be caused by summing many different velocity components around the center, whose distributions are unresolved with the beam size of $\sim 0.08''$. The merged spectra could lead to the widely different ratios of the optical depth of the systemic components to redshifted, e.g., 1.12 for $F = 4 - 4$ and 0.34 for $F = 5 - 5$. To investigate the line ratio in more detail, observations with higher angular resolution enough to resolve the distribution of the OH $^2\Pi_{3/2}$ $J = 9/2$ lines would be needed.

Table 5. The observed flux densities of NH_3 $(1,1)-(6,6)$ and 24-GHz continuum with VLA (this work) and GBT. Values in parentheses are standard deviations.

	NH_3						
Telescope	$(1,1)$	$(2,2)$	$(3,3)$	$(4,4)$	$(5,5)$	$(6,6)$	Continuum
	Systemic Components (mJy)						(mJy)
VLA	−8.15(0.22)	−10.28(0.38)	−1.23(0.38)	−9.18(0.31)	−7.34(0.28)	−10.00(0.36)	50
GBT*	−18.51(0.64)	−22.55(0.59)	...	−19.47(0.69)	−11.97(0.69)	−13.67(0.96)	174
$\lvert S_{\rm GBT}/S_{\rm VLA}\rvert$	2.27(0.10)	2.19(0.10)	...	2.12(0.10)	1.63(0.11)	1.37(0.11)	3.5
	Blueshifted Components (mJy)						
VLA	−1.75(0.18)	−2.34(0.27)	1.54(0.45)	−1.60(0.20)	−1.23(0.15)	−2.07(0.24)	
GBT*	−3.40(0.64)	−4.26(0.59)	...	−3.46(0.69)	−2.45(0.69)	−1.33(0.96)	
$\lvert S_{\rm GBT}/S_{\rm VLA}\rvert$	1.95(0.42)	1.82(0.33)	...	2.16(0.51)	1.99(0.61)	0.64(0.47)	

* GBT data are from Mangum et al. (2013).

Table 6. The emission lines close to $NH_3(3,3)$

Transitions	Rest frequency (GHz)	ΔV (km s^{-1})*
H(81)β	23.86086	117
$NH_3(3,3)$	23.87013	—
He(81)β	23.87059	−6
		Emission velocity range (km s^{-1})†
$NH_3(3,3)$	23.87013	835–1045
H(80)β	24.75574	$\simeq$ 718–928
He(80)β	24.76583	$\simeq$ 841–1051

* Velocity difference relative to the rest frequency of $NH_3(3,3)$.

† Estimated velocity range in H(80)β and He(80)β in case that the emission features in figure 5 are caused by H(81)β and He(81)β, respectively.

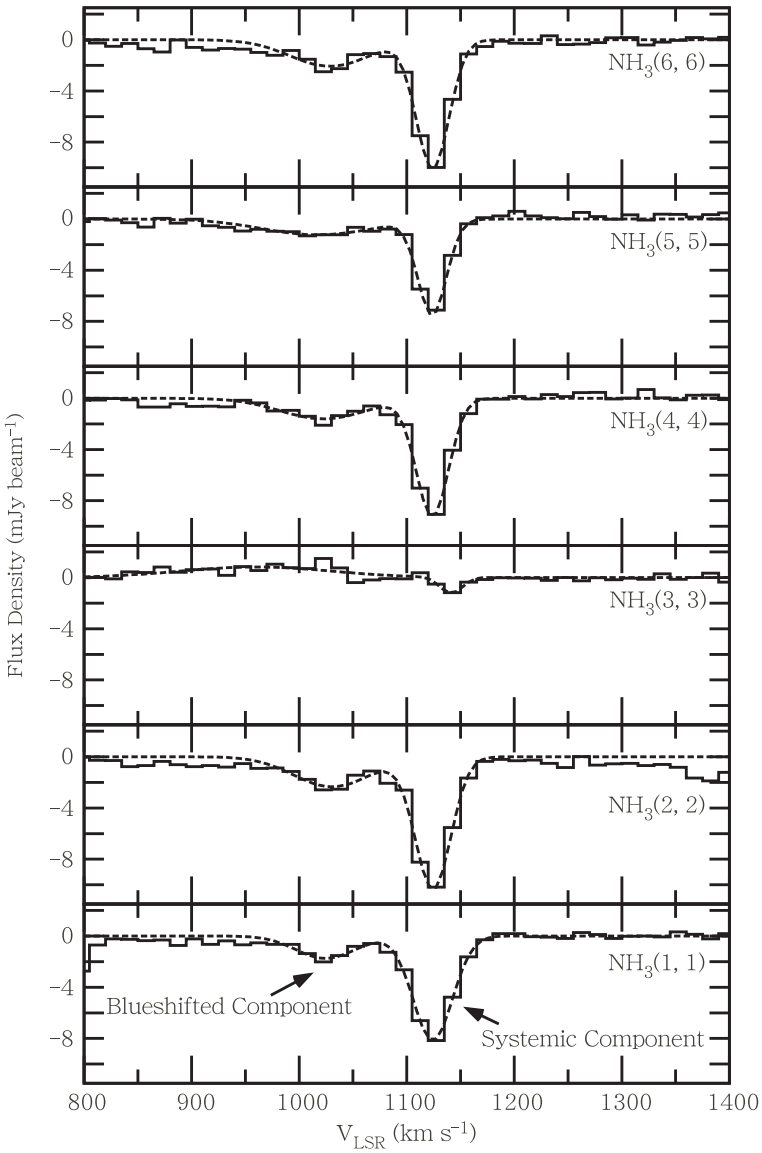

Fig. 3. Continuum-subtracted NH_3 lines at the center of NGC 3079 with the VLA. The spectra of $NH_3(J,K) = (1,1)$, $(2,2)$, $(3,3)$, $(4,4)$, $(5,5)$, and $(6,6)$ from bottom to top. Gaussian fits to the lines are overlaid with dotted lines.

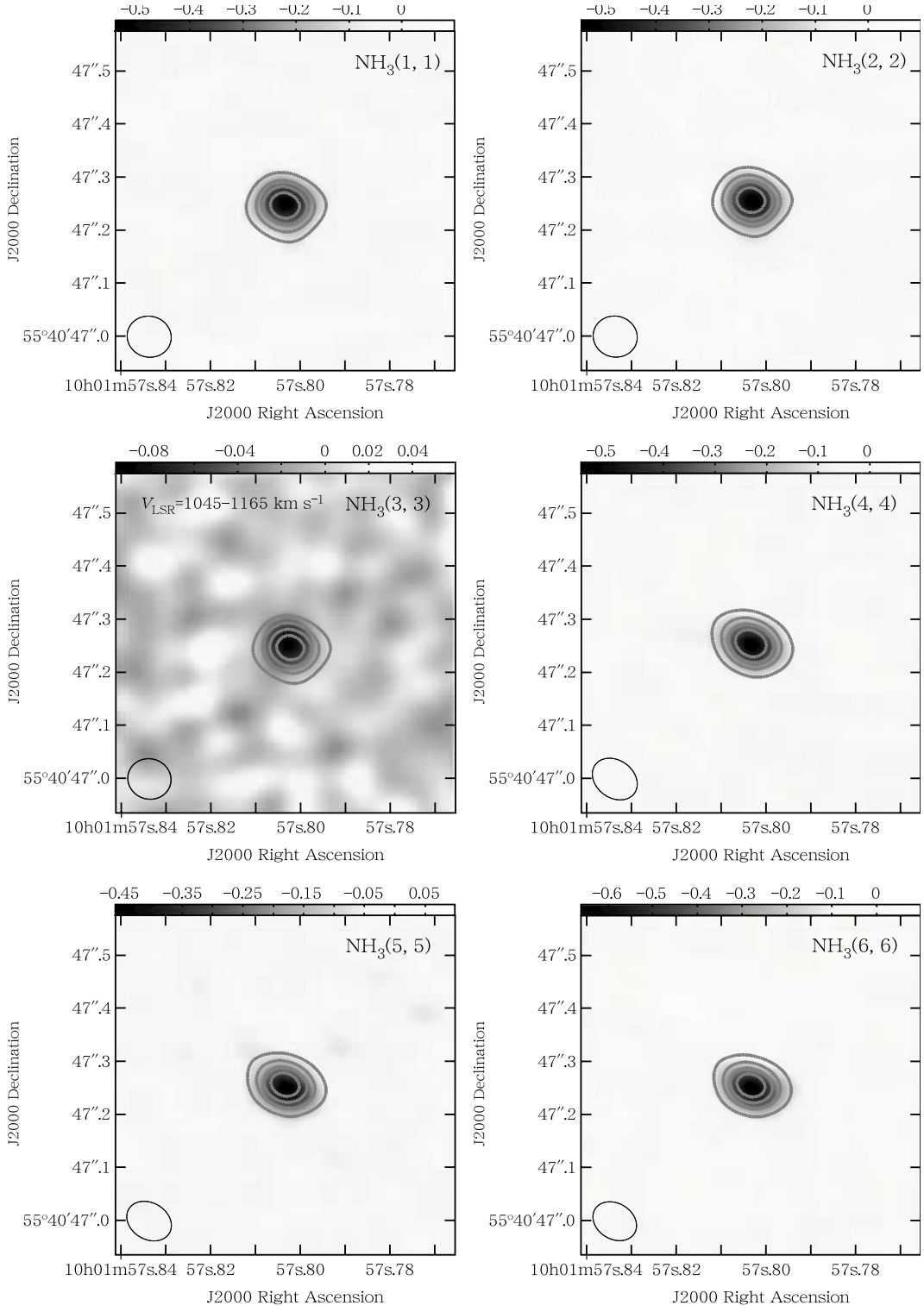

Fig. 4. The continuum map (contours) extracted from the absorption-free regions in band is superposed on the integrated intensity map (Jy beam^{-1} km s^{-1}) of $NH_3(1,1)$ to (6,6) absorption lines (color). The integrated velocity ranges of $NH_3(1,1)$, (2,2), (4,4), (5,5) and (6,6) lines are $V_{\rm LSR} = 835$–1180 km s^{-1}, and that of $NH_3(3,3)$ is $V_{\rm LSR} = 1045$–1165 km s^{-1}. The contours are plotted at 10, 20, 30 and 40 mJy beam^{-1}. The synthesized beam is plotted at the lower left corner.

Table 7. OH parameters

Transitions	S^* (mJy)	$V_{\rm LSR}{}^*$ (km s^{-1})	$\Delta v_{1/2}$ (km s^{-1})	τ^*	$\int \tau dv$ (km s^{-1})	$S_{\rm cont}$(rms noise) (mJy)
OH $^2\Pi_{2/3} J = 9/2$	Systemic Components					
$F = 4 - 4$	-2.23 ± 0.16	1085 ± 4	98 ± 8	0.046 ± 0.003	4.75 ± 0.53	49.99 (0.28)
$F = 5 - 5$	-1.25 ± 0.10		193 ± 19	0.025 ± 0.002	5.21 ± 0.67	
	Refshifted Components					
$F = 4 - 4$	-2.00 ± 0.14	1302 ± 2	62 ± 6	0.041 ± 0.003	2.68 ± 0.34	
$F = 5 - 5$	-3.51 ± 0.14		107 ± 7	0.073 ± 0.003	8.31 ± 0.64	

*Values at the absorption peak after Gaussian fitting.

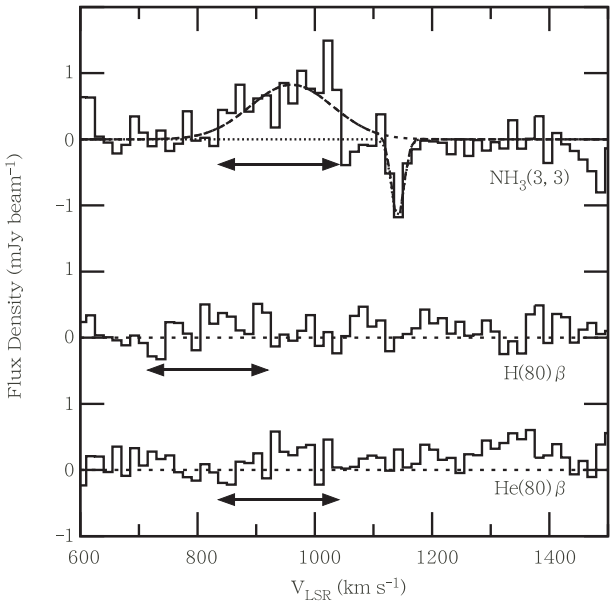

Fig. 5. Enlargement of the $NH_3(3,3)$ spectrum in figure 3, and H(80)β and He(80)β spectra for comparison are shown. If the emission line in the frame of $NH_3(3,3)$ is attributed to the H(81)β or He(81)β line, the H(80)β or He(80)β line should be appeared in the range shown by the horizontal arrows, but no significant emission can be seen, indicating that the emission at $V_{\rm LSR} \approx 830$–1050 km s^{-1} is not H(81)β and He(81)β but $NH_3(3,3)$.

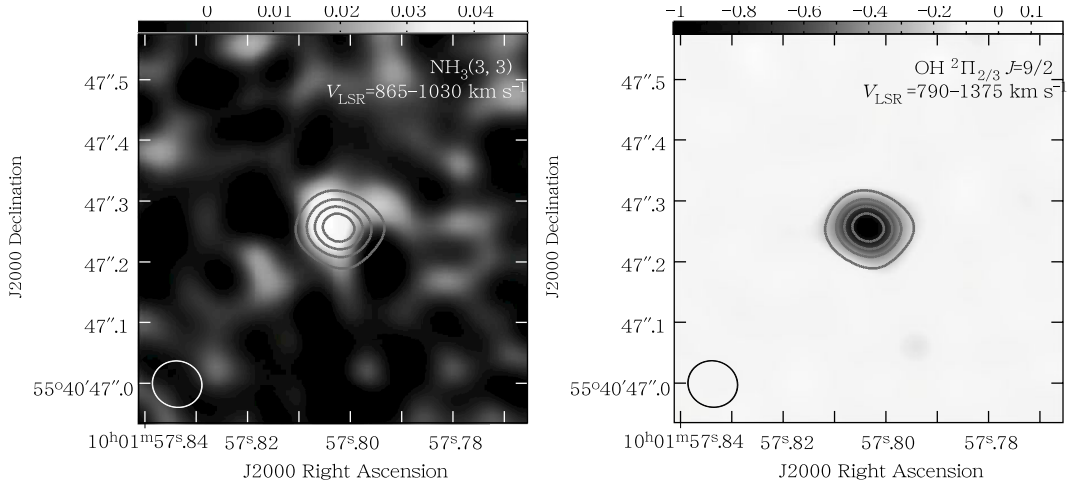

Fig. 6. The integrated intensity map of the blueshifted features of $NH_3(3,3)$ (left) and the OH $^2\Pi_{3/2}$ $J = 9/2$ absorption line (right). The continuum map (contours) is the same as that of the systemic features of $NH_3(3,3)$ in figure 4.

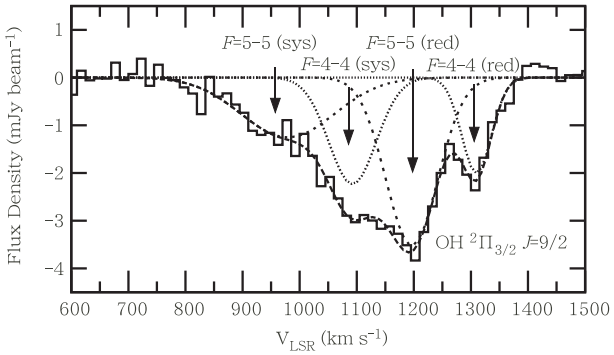

Fig. 7. The absorption spectrum of OH $^2\Pi_{3/2} J = 9/2$. Gaussian fits to the lines are overlaid. The velocity is referenced to $\nu = 23.8176153$ of OH $^2\Pi_{3/2} J = 9/2$ $F = 4 - 4$.

4. Discussion

4.1. The possibility of $NH_3(3,3)$ maser

It has been reported that distributions of $NH_3(3,3)$ masers and H_2O masers in the massive star forming regions are associated each other, because the $NH_3(3,3)$ masers are formed by shocks due to the interaction of molecular outflows with the ambient gas in, e.g., NGC 6334 (Kraemer & Jackson 1995), DR21 (Zhang & Ho 1995). VLBI observations of H_2O maser toward the center of NGC 3079 also strongly support the possibility of the NH_3 maser. Yamauchi et al. (2004) found exceptionally strong blueshifted H_2O maser features at the nearly same velocities of $V_{\rm LSR} \approx 900$–1050 km s^{-1} as our blueshifted components, showing peculiar motion (LSM1 and LSM2 in their paper) that does not follow the rotation of the nuclear maser disk. The velocity and spatial distributions of the maser spots suggested two expanding partial shells in

the massive and geometrically thick maser disk and located at about 7 mas (0.7 pc; LSM2) and 13 mas (1.2 pc; LSM1) from the nucleus, being probably formed by local shock related to star formation (Yamauchi et al. 2004). These results strongly suggest that the emission features of $NH_3(3,3)$ are caused by the $NH_3(3,3)$ maser associated with shocks by winds from newly formed massive stars or supernova explosions in extremely dense clouds in the nuclear region of NGC 3079, although the distribution of the $NH_3(3,3)$ maser is unresolved with the angular resolution of $\sim 0\farcs1$ [see figure 6 (left)]. The blueshifted absorption features of $NH_3(1,1)$, $(2,2)$ and (4.4)–$(6,6)$ at the same velocities could be also caused by the dense molecular gas in the nuclear H_2O maser disk.

Absorption features of para-NH_3 have been found in IC 860, NGC 253, NGC 660, NGC 3079 and Arp 220 (Mangum et al. 2013; Ott et al. 2005; Takano et al. 2005; Ott et al. 2011), while maser emission of $NH_3(3,3)$ has been detected only in NGC 253 and NGC 3079 (Ott et al. 2005; Mangum et al. 2013). Ott et al. (2005) speculated that the maser emission in NGC 253 was associated with the star forming region. Measurements of the brightness temperature and distribution of the emission with VLBI could determine if the emission of $NH_3(3,3)$ is masers associated with star formation.

4.2. Rotational Temperatures of NH_3

In the case of an absorption line, the optical depth can be derived from the brightness temperature of the line ($T_{\rm L}$) relative to the measured brightness temperature of the background continuum $T'_{\rm C}(= f_{\rm C}T_{\rm C})$ as below (e.g., Hüttemeister et al. 1993; Ott et al. 2011),

$$\tau = -\ln\left(1 - \frac{|T_{\rm L}|}{T'_{\rm C}}\right), \tag{2}$$

where $T_{\rm C}$ is the continuum brightness temperature and $f_{\rm C}$ the beam filling factor of the continuum source whose individual emitting regions are small as shown with VLBI (e.g., Trotter et al. 1998; Yamauchi et al. 2004) and thus which is assumed to be fully covered by the molecular gas. The resultant peak optical depths of NH_3 and OH are given in table 4 and 7, respectively. Using the optical depth, the NH_3 column density divided by the excitation temperature ($T_{\rm ex}$) for the inversion doublet can be expressed by

$$\frac{N(J,K)}{T_{\rm ex}} = 1.65 \times 10^{14} \frac{J(J+1)}{K^2 \nu} \tau \Delta v_{1/2}\ [{\rm cm^{-2}K^{-1}}], \tag{3}$$

as in Mauersberger et al. (1986), where ν is the transition frequency in GHz and $\Delta v_{1/2}$ the line width (FWHM) in km s^{-1}. The NH_3 populations are described by two temperatures, one is the excitation temperature $T_{\rm ex}$ which characterizes the population across a (J,K) inversion doublet and the other the rotational temperature $T_{\rm rot}$ which characterizes the populations of energy levels with different (J,K). Since the populations of metastable inversion levels are determined by collisions, there is a direct relation between $T_{\rm rot}$ and the kinetic temperature $T_{\rm k}$. The column density divided by $T_{\rm ex}$ as a function of energy is described by the Boltzmann law

with a specific $T_{\rm rot(J',K';J,K)}$,

$$\frac{N(J',K')/T'_{\rm ex}}{N(J,K)/T_{\rm ex}} = \frac{g_{\rm op'}}{g_{\rm op}} \frac{(2J'+1)}{(2J+1)} \exp\left(-\frac{\Delta E}{T_{\rm rot(J',K';J,K)}}\right), \quad (4)$$

as in Ott et al. (2011), where ΔE is the energy difference between the rotational states (J',K') and (J,K) in K, and $g_{\rm op}$ the statistical weight factor [$g_{\rm op}=1$ for para-NH_3 ($K \neq 3n$) and $K=0$, and $g_{\rm op}=2$ for ortho-NH_3 ($K=3n$)].

The rotational temperature can be derived from the rotational diagram (figure 8), which is the logarithmic plot of the normalized column densities, $\log[N(J,K)/(T_{\rm ex}(2J+1)g_{\rm op})]$ as a function of energy levels corresponding to the transitions. Here we treat ortho- and para-NH_3 separately, because the transitions between ortho- and para-NH_3 are not allowed and hence the two behave independently. The rotational temperatures for the systemic component derived from two transitions of $NH_3(1,1)$–$(2,2)$ and $(4,4)$–$(5,5)$ are $T_{\rm rot\ (11,22)} = 64 \pm 5$ K and $T_{\rm rot\ (44,55)} = 164 \pm 14$ K. This indicates that the systemic components consist of at least two temperature components, like the center of the Galaxy (e.g., Hüttemeister et al. 1995; Mills & Morris 2013) and the other galaxies, (e.g., NGC 1068: Ao et al. 2011). The presence of two temperature components in the central region of NGC 3079, i.e., the hot molecular gas ($T_{\rm k}=150$ K, $n_{\rm H_2}=10^3$ cm^{-3}) and the cold dense gas ($T_{\rm k}=20$ K, $n_{\rm H_2}=10^4$ cm^{-3}), was also shown by the radiative transfer model using multi-transition of ^{12}CO and ^{13}CO lines with single dishes ($\theta \sim 23''$ in CO(1–0); Israel 2009). Moreover in figure 8, the larger column density of $NH_3(6,6)$, whose energy level is 408 K, than the value extrapolated from the lower transition lines indicates the existence of the hotter gas.

We also derived the mean rotational temperature of $T_{\rm rot} = 120 \pm 12$ K for the systemic features, using para-NH_3 lines, $(1,1)$, $(2,2)$, $(4,4)$ and $(5,5)$, for comparing with other galaxies. The derived rotational temperature is consistent with the previous results of NGC 3079 [$T_{\rm rot} >$ 106 K, derived from the same para-NH_3 lines in Mangum et al. (2013)], and is higher than temperatures in other galaxies already reported (e.g., $T_{\rm rot} = 44^{+6}_{-4}$ K in NGC 1068; Ao et al. 2011). The rotational temperature of the blueshifted component was evaluated to be $T_{\rm rot} = 157 \pm 19$ K from the para-NH_3 lines.

The kinetic temperature ($T_{\rm k}$) is, in general, higher than the rotational temperature (Walmsley & Ungerechts 1983). The relation between $T_{\rm rot}$ and $T_{\rm k}$, which was derived from radiative transfer large velocity gradient (LVG) models, was shown by Ott et al. (2011) for ammonia rotational transitions. We roughly estimate the mean kinetic temperature of $T_{\rm k} = 270 \pm 60$ K for the systemic components using the mean rotational temperature, $T_{\rm rot} = 120$ K, and the relation between $T_{\rm k}$ and $T_{\rm rot\ (22,44)}$ (figure 5 in Ott et al. 2011). For the blueshifted components, we can derive the lower limit of the kinetic temperature, $T_{\rm k} > 500$ K.

4.3. Rotational Temperature of OH

We also estimated the rotational temperature of the systemic component of OH from the ratio of the normalized column density between $^2\Pi_{3/2}$ $J = 3/2$ and $J = 9/2$, assuming that the systemic components of OH $^2\Pi_{3/2}$ $J = 3/2$ in the 1667- and 1665-MHz transitions (Hagiwara et al. 2004) are emitted from the same region as that of OH $^2\Pi_{3/2}$ $J = 9/2$. The normalized OH column density is expressed as (Baudry et al. 1981),

$$\frac{N_l}{T_{\rm ex}} = 2.07 \times 10^3 \nu^2 \frac{g_l}{g_u} A_{ul}^{-1} \tau \Delta v_{1/2} \ [{\rm cm^{-2}\ K^{-1}}], \tag{5}$$

where N_l is the column density of one ($F = 4$–4 or 5–5) of the two hyperfine levels at the lower state of the Λ-doublet, ν the frequency of the transition in GHz, A_{ul} the Einstein A-coefficient (Destombes et al. 1977), and g_l and g_u are the statistical weights $(2F + 1)$ of the lower and upper levels, respectively. Since the mean total column density of $J = 9/2$ is given by

$$\frac{N_{9/2}}{T_{\rm ex}} = 7.46 \times 10^{13} \tau_{4-4} \Delta v_{1/2} + 7.42 \times 10^{13} \tau_{5-5} \Delta v_{1/2} \ [{\rm cm^{-2}\ K^{-1}}], \tag{6}$$

as in Baudry & Menten (1995), we obtain $N_{9/2}/T_{\rm ex} = 6.98 \times 10^{14}$ cm^{-2} K^{-1} for the systemic component, using the parameters of τ and $\Delta v_{1/2}$ for $F = 4$–4 and 5–5 in table 7. The rotational temperature of $T_{\rm rot,OH} \sim 175$ K between $J = 9/2$ and $J = 3/2$ was derived from the equation,

$$\left(N_{9/2}/T_{\rm ex}\right) / \left(N_{3/2}/T'_{\rm ex}\right) = (10/4) \exp(-\Delta E/T_{\rm rot}) \ , \tag{7}$$

where $N_{3/2}/T'_{\rm ex} = 5.3 \times 10^{15}$ cm^{-2} K^{-1} (Hagiwara et al. 2004). The rotational temperature of OH has large uncertainty because the velocities of the systemic components between OH $^2\Pi_{3/2}$ $J = 3/2$ and OH $^2\Pi_{3/2}$ $J = 9/2$ lines are not exactly same [compare our figure 7 with figure 1 of Hagiwara et al. (2004)]. It is expected that the rotational temperature of the redshifted component could be higher than that of the systemic, because the OH $^2\Pi_{3/2}$ $J = 3/2$ in ground state was not detected but the $^2\Pi_{3/2}$ $J = 9/2$ whose energy level is 511 K.

4.4. Distribution of molecular gas in the nuclear region

Figure 9 shows the distribution of the peak positions of NH_3 and OH lines for the systemic and blueshifted components in the coordinate system relative to the position of R.A. (J2000.0)= $10^{\rm h}01^{\rm m}57\overset{\rm s}{.}8034$, Decl. (J2000.0)= $55^\circ40'47\overset{''}{.}243$ determined from observations with VLBI (Petrov & Taylor 2011). The statistic position errors were evaluated from $\Delta\theta = 0.5\ \theta_{\rm beam}/SNR$ (e.g., Moran et al. 1999), where $\theta_{\rm beam}$ is the synthesized beam size (table 2) and SNR the signal-to-noise ratio of the peak absorption. The circles in figure 9 show the positions of the peak intensities of the $NH_3(1,1)$, (2,2), (4,4), (5,5) and (6,6) absorption integrated with 2 and 3 channels, corresponding to $V_{\rm LSR} = 1105$–1135 km s^{-1} and 1000–1045 km s^{-1}, for the systemic and blueshifted components, respectively. The peak positions of the $NH_3(3,3)$ lines integrated with $V_{\rm LSR} = 1120$–1165 km s^{-1} for the systemic components (absorption) and 970–1045 km s^{-1} for the blueshited (emission) are also plotted.

In figure 9, the systemic and blueshifted features, with the exception of blueshifted $NH_3(1,1)$ and $(3,3)$ are located at the north-west and south-east relative to the reference center, respectively. A least-squares fitting of the systemic and blueshifted components gives $P.A. \approx -53°$, in agreement with the position angle of the nuclear continuum jet measured with VLBI ($P.A. = -52°$, Trotter et al. 1998; Yamauchi et al. 2004), suggesting that ammonia is absorbed against the continuum emission of the nuclear jet. The velocity structure of NH_3 absorption is inconsistent with the kpc-scale galactic disk and the pc-scale nuclear water maser disk with $P.A. = -8°$ which rotates with the northern side approaching and the southern receding (Yamauchi et al. 2004), but is nearly consistent with that of OH absorption at 1665-MHz (Hagiwara et al. 2004). The projected separation between the averaged positions of the systemic and blueshifted components in figure 9, 8.6 mas, is also consistent with the position offsets of $\sim$ 7–8 mas between two peaks of the systemic and blueshifted components of the OH absorption (Hagiwara et al. 2004). The blueshifted absorption features of NH_3 and OH could be explained with an association with molecular outflows possibly caused by the jet, as suggested by Hagiwara et al. (2004).

On the other hand, the relative position of the blueshifted $NH_3(3,3)$ emission is located at $\sim$10 mas north of the nuclear jet, in agreement with the positions of the H_2O masers (LSM2) formed by local shocks related to star formation in the nuclear maser disk (Yamauchi et al. 2004). The position of the blueshifted $NH_3(1,1)$ close to the $NH_3(3,3)$ could be explained by the enhancement of NH_3 due to the local shock (e.g., Draine & McKee 1993; Flower et al. 1995).

Figure 9 also shows the peak positions of the systemic and redshifted components of the OH $^2\Pi_{3/2}$ $J = 9/2$ $F = 4$–4 and $F = 5$–5 lines, where the velocity ranges of $V_{\rm LSR} = 1075$–1105 km s^{-1} and 1285–1315 km s^{-1} are adopted for the systemic and redshifted components of the $F = 4$–4 line, and $V_{\rm LSR} = 970$–1000 km s^{-1} and 1180–1210 km s^{-1} for the systemic and redshifted of the $F = 5 - 5$ line. The peak positions of the systemic components of the $F = 4$–4 and $F = 5$–5 are located close to the positions of the systemic NH_3 lines. The redshifted component of the OH $F = 5$–5 is located at the northwestern side with respect to the systemic components of the OH $F = 4$–4, 5–5, and NH_3 lines aligned along the nuclear jet. The redshifted component of the OH $F = 4$–4 line is however at the further northern side near the shock gas region of H_2O masers (Yamauchi et al. 2004) and the blueshifted component of $NH_3(3,3)$. To make the distributions of these molecular gas clear, observations with higher angular resolution, e.g, with VLBI would be needed.

4.5. Abundance of Ammonia

In order to derive column densities of NH_3 from the absorption lines, the excitation temperature $T_{\rm ex}$ is required, as shown in equation (3). Although radiative transfer models are needed to determine $T_{\rm ex}$ (e.g., Walmsley & Ungerechts 1983), we estimated the column

densities for the systemic and blueshifted components, assuming $T_{\rm ex} \approx T_{\rm rot} (< T'_{\rm C} \sim 1.7 \times 10^4$ K; $T'_{\rm C}$ = the brightness temperature of the background continuum source). The ortho-$NH_3(0,0)$ does not exhibit an inversion line and $(3,3)$ is degenerated by the contamination of the maser emission (subsection 3.2.2), and hence we extrapolate the column densities of $NH_3(0,0)$ and $(3,3)$ from the rotational temperature for para-NH_3 and $N/T_{\rm ex}$ of $NH_3(6,6)$ in figure 8. The derived column densities of the systemic and blueshifted components are summarized in table 8.

The fractional abundances of $\sum_{J=0}^{6} N_J$ (NH_3) relative to the column densities of H_2 for the systemic and blueshifted components are $[NH_3]/[H_2] = 1.3 \times 10^{-7}$ and 6.5×10^{-8}, respectively, where the column density of H_2 ($= 6.8 \times 10^{23}$ cm^{-2}) is estimated from the CO integrated intensity, $I_{\rm CO} \equiv \int T_b \, dv$, with the angular resolution of $1\farcs9$ (Koda et al. 2002) and the conversion factor of $X \equiv N(H_2)/I_{\rm CO} = 1.8 \times 10^{20}$ cm^{-2} (K km s^{-1})$^{-1}$ (Dame et al. 2001). It is difficult to decide whether the difference of the abundance between the systemic and blueshifted components by a factor of two is real, because the column densities of $NH_3(3,3)$ estimated only from that of $NH_3(6,6)$ and $T_{\rm rot}$ of para-NH_3 occupy 46 % and 42 % of the total column densities of the systemic and blueshifted component, respectively, maybe causing the uncertainty of nearly a factor of two for the difference.

In the central regions ($r \leq 0.17$–1.1 kpc) of other galaxies, the fractional abundance of ammonia was $(1.3$–$2.9) \times 10^{-8}$ for NGC 253, IC 342, Maffei 2 and NGC 1068, 4.5×10^{-9} for M51, and 5×10^{-10} for M82 (see Takano et al. 2013 and references therein). The ammonia abundance, at least of the systemic component (1.3×10^{-7}), in the nuclear region of NGC 3079 is higher than that of the other galaxies, even if the uncertainty of the density of $NH_3(3,3)$ is considered. To know the reason of the high abundance in NGC 3079, it would be important to measure the ammonia abundance in the nuclear regions of other galaxies, especially active galactic nuclei having jet, from observations with high resolutions of $r \leq 10$ pc.

5. Conclusions

We reported the results of ammonia observations toward the center of NGC 3079 with the Tsukuba 32-m telescope and VLA. The main conclusions are summarized as follows:

1. We detected ammonia $(J,K) = (1,1)$ and $(2,2)$ inversion lines in absorption with the Tsukuba 32-m, and $(J,K) = (1,1)$ through $(6,6)$ lines with the VLA although the profile of the $NH_3(3,3)$ line was anomalous.
2. We detected an unresolved continuum source with the resolution of $\lesssim 0\farcs09 \times 0\farcs08$. On the other hand, the flux density of ~ 50 mJy is smaller than the flux obtained by observations with the GBT, and larger than that with VLBI. These results indicate that the continuum source is extended more than $r \sim 1''$.
3. All ammonia absorption lines have two distinct velocity components: one is at the systemic velocity and the other is blueshifted, and align along the nuclear jet. For the systemic

Table 8. Ammonia rotational temperatures and column densities

	Systemic component	Blueshifted component
$T_{\rm rot}$	120 ± 12 K	157 ± 19 K
	Column density* $[\times 10^{15}$ cm$^{-2}]$	
$NH_3(0,0)$	$(4.6 \pm 0.5)^{\dagger}$	$(1.9 \pm 0.2)^{\dagger}$
$NH_3(1,1)$	12.5 ± 0.5	5.0 ± 0.8
$NH_3(2,2)$	11.0 ± 0.7	6.5 ± 1.4
$NH_3(3,3)$	$(41.1 \pm 4.1)^{\dagger}$	$(19.0 \pm 2.3)^{\dagger}$
$NH_3(4,4)$	7.0 ± 0.4	4.0 ± 1.0
$NH_3(5,5)$	4.8 ± 0.3	3.8 ± 1.2
$NH_3(6,6)$	7.5 ± 0.5	4.5 ± 1.0
$\sum_{J=0}^{6} N$	88.5 ± 7.0	44.7 ± 7.8

*Assumed $T_{\rm ex} \approx T_{\rm rot}$.

†Brackets are values extrapolated from $T_{\rm rot}$ for para-ammonia and $N/T_{\rm ex}$ of $NH_3(6,6)$.

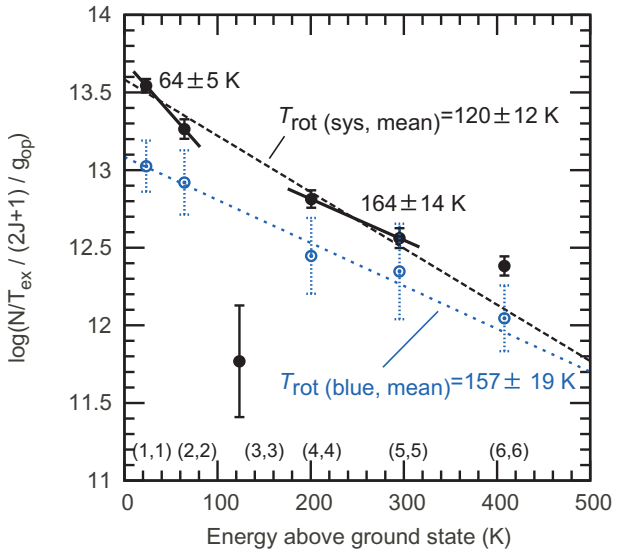

Fig. 8. Rotational diagram of the ammonia measurements. The ordinate exhibits the logarithm of normalized $N/T_{\rm ex}$. The systemic and blueshifted components are marked by filled and open circles, respectively. The thick and thin dotted lines indicate the results of the least-square fitting of the systemic and blueshifted components, respectively, for $(J,K) = (1,1),(2,2),(4,4)$ and $(5,5)$. The mean rotational temperatures for the systemic and blueshifted features are shown. In addition, the rotational temperatures derived from two transitions of $NH_3(1,1)$–$(2,2)$ and $(4,4)$–$(5,5)$ for the systemic component are shown.

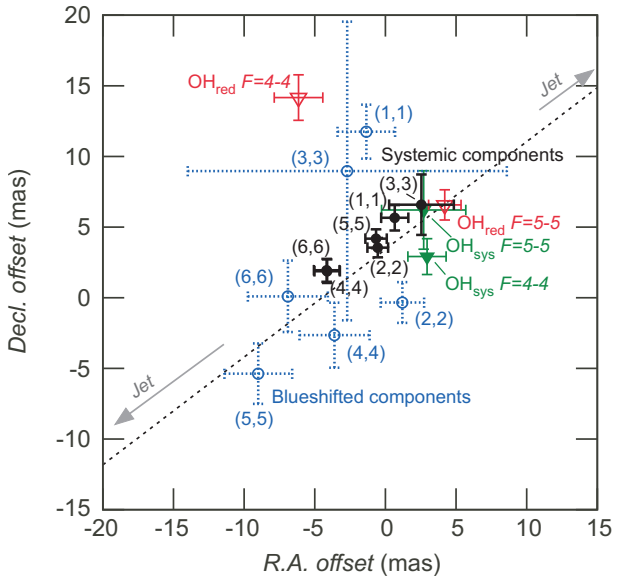

Fig. 9. Distribution of NH_3 lines in the nuclear region of NGC 3079. The origin of the coordinates is R.A. (J2000.0)= $10^h01^m57^s.8034$, Decl. (J2000.0)= $55°40'47''.243$ (Petrov & Taylor 2011). Filled and open circles indicate the peak positions of $NH_3(1,1)$–$(6,6)$ for the systemic and blueshifted components, respectively. A dashed line with a position angle of $P.A. = -53°$ is the result of a least-squares fitting of the positions with the exception of blueshifted $NH_3(1,1)$ and $(3,3)$. Filled triangles show the peak positions of the systemic components of OH $^2\Pi_{3/2}$ $J = 9/2$ $F = 4$–4 and $F = 5$–5, and open triangles those of the redshifted.

components, the ratio of the flux densities with GBT to VLA decreases with the excitation level, indicating that the relatively low temperature gas is more extended than the high temperature gas.

4. At the blueshifted velocity, the $NH_3(3,3)$ line shows emission feature. The blueshifted feature is consistent with the distribution and velocity of the H_2O maser formed by local shock related to star formation. We regarded $NH_3(3,3)$ maser as the most likely candidate of the emission, and suggested that the maser was associated with shocks by strong winds from newly formed massive stars or supernova explosions in dense clouds in the nuclear region of NGC 3079.
5. Using para-$NH_3(1,1)$, (2, 2), (4, 4) and (5, 5) lines with the VLA, we derived the rotational temperature $T_{\rm rot} = 120 \pm 12$ K and 157 ± 19 K for the systemic and blueshifted components, respectively. The temperatures correspond to the kinetic temperatures of $T_{\rm k} = 270 \pm 60$ K and > 500 K for the systemic and blueshifted components, respectively.
6. Combined column densities of the measured lines plus the extrapolated $(0,0)$ column become $(8.85 \pm 0.70) \times 10^{16}$ cm^{-2} and $(4.47 \pm 0.78) \times 10^{16}$ cm^{-2} for the systemic and blueshifted components, respectively, assuming $T_{\rm ex} \approx T_{\rm rot}$. The fractional abundances of $\sum_{J=0}^{6} N_J$ (NH_3) relative to the column densities of H_2 for the systemic and blueshifted components are $[NH_3]/[H_2] = 1.3 \times 10^{-7}$ and 6.5×10^{-8}, respectively.

7. We found an absorption which is likely to be caused by the $F = 4$–4 and $F = 5$–5 doublet of OH $^2\Pi_{3/2}$ $J = 9/2$. Given that each doublet line has same velocity components, the wide absorption feature can be fitted by two velocity components. These velocity components are different from the velocities at the ground state of OH $^2\Pi_{3/2}$ $J = 3/2$ and NH_3, not showing the blueshifted components but the redshift. We estimated the rotational temperature of $T_{\rm rot,OH} \gtrsim 175$ K from OH $^2\Pi_{3/2}$ data. The highly excited OH line can trace hot gas associated with the interaction of the fast nuclear outflow with dense and dusty molecular material around the nucleus.

We thank the members of the observational astrophysics group of the University of Tsukuba for participating in the construction of the K-band observing system of the Tsukuba 32-m telescope. We are grateful to the VLBI group of the Geospatial Information Authority of Japan (GSI) geodetic department for licensing to use the 32-m telescope. The observations with the 32-m telescope have been made under the agreement on the collaboration between the University of Tsukuba and the GSI. This work was supported in part by JSPS (Japan Society for the Promotion of Science) KAKENHI Grant Numbers 173400052, 17654042, 20244011 and 26247019. The National Radio Astronomy Observatory is a facility of the National Science Foundation operated under cooperative agreement by Associated Universities, Inc. This research has made use of the NASA/IPAC Extragalactic Database (NED) which is operated by the Jet Propulsion Laboratory, California Institute of Technology, under contract with the National Aeronautics and Space Administration. Some of the data presented in this paper were obtained from the Mikulski Archive for Space Telescopes (MAST). STScI is operated by the Association of Universities for Research in Astronomy, Inc., under NASA contract NAS5-26555. Support for MAST for non-HST data is provided by the NASA Office of Space Science via grant NNX13AC07G and by other grants and contracts.

References

Ao, Y., Henkel, C., Braatz, J. A., Weiß, A., Menten, K. M. & Mühle, S. 2011, A&A, 529, 154
Baan, W. A. & Irwin, J. A. 1995, ApJ, 446, 602
Baudry, A., Walmsley, C. M., Winnberg, A. & Wilson, T. L. 1981, A&A, 102, 287
Baudry, A. & Menten, K. M. A&A, 298, 905
Braine, J., Guelin, M., Dumke, M., Brouillet, N., Herpin, F. & Wielebinski, R. 1997, A&A, 326, 963
Brunthaler, A., Castangia, P., Tarchi, A., Henkel, C., Reid, M. J., Falcke, H. & Menten, K. M. 2009, A&A, 497, 103
Cecil, G., Bland-Hawthorn, J., Veilleux, S. & Filippenko, A. V. 2001, ApJ, 555, 338
Dame, T. M., Hartmann, D., & Thaddeus, P. 2001, ApJ, 547, 792
Danby, G., Flower, D. R., Valiron, P., Schilke, P. & Walmsley, C. M. 1988, MNRAS, 235, 229
de Pater, I., Gibbard, S. G., Chiang, E., Hammel, H. B., Macintosh, B., Marchis, F., Martin, S. C.,

Roe, H. G. & Showalter, M. 2005, Icarus, 174, 263
Destombes, J. L., Marliere, C., Baudry, A., & Brillet, J. 1977, A&A, 60, 55
de Vaucouleurs, G., de Vaucouleurs, A., Corwin, Jr., H. G., Buta, R. J., Paturel, G. & Fouqué, P. 1991, Third Reference Catalogue of Bright Galaxies (Springer, New York)
Draine, B. T. & McKee, C. F. 1993, ARA&A, 31, 373
Duric, N., & Seaquist, E., 1988, ApJ, 326, 574
Flower, D. R., Pineau des Forets, G. & Walmsley, C. M. 1995, A&A, 294, 815
Ford, H. C., Dahari, O., Jacoby, G. H., Crane, P. C. & Ciardullo, R, 1986, ApJ, 311, L7
Guilloteau, S., Baudry, A., Walmsley, C. M., Wilson, T. L. & Winnberg, A. 1984, A&A, 131, 45
Hagiwara, Y., Klöckner, H.-R. & Baan, W., 2004, MNRAS, 353, 1055
Hawarden, T. G., Israel, F. P., Geballe, T.R. & Wade, R., 1998, MNRAS, 276, 1197
Heckman, T. M. 1980, A&A, 87, 152
Heckman, T. M., Armus, L. & Miley, G. K. 1990, ApJS, 74, 833
Henkel, C., Mauersberger, R., Peck, A. B., Falcke, H. & Hagiwara, Y. 2000 A&A, 361, 45
Hüttemeister, S., Wilson, T. L., Henkel, C. & Mauersberger, R. 1993, A&A, 276, 445
Hüttemeister, S., Wilson, T. L., Mauersberger, R., Lemme, C., Dahmen, G. & Henkel, C., 1995, A&A, 300, 636
Irwin, J. A. & Seaquist, E. R. 1986, ApJ, 371, 111
Irwin, J. A. & Sofue, Y. 1992, ApJ, 396, 75
Israel, F. P., van der Werf, P. P., Hawarden, T. G., & Aspin, C., 1998, A&A, 336, 433
Israel, F. P. 2009, A&A, 493, 525
Koda, J., Sofue, Y., Kohno, K., Nakanishi, H., Onodera, S., Okumura, S. K. & Irwin, J. A., 2002, ApJ, 573, 105
Kohno, K., Matsushita, S., Vila-Vilaró, B., Okumura, S. K., Shibatsuka, T., Okiura, M., Ishizuki, S. & Kawabe, R. 2001, ASPC, 249, 672
Kraemer, K. E. & Jackson, J. M., 1995, ApJ, 439L, 9
Mangum, J. G., Darling, J., Henkel, C., Menten, K. M., MacGregor, M., Svoboda, B. E., Schinnerer, E., 2013, ApJ, 779, 33
Mauersberger, R., Henkel, C., Wilson, T. L. & Walmsley, C. M. 1986b, A&A, 162, 199
McMullin, J. P., Waters, B., Schiebel, D.,Young, W., & Golap, K., 2007, Astronomical Data Analysis Software and Systems XVI, 376, 127
Meaburn, J., Fernandez, B. R., Holloway, A. J., Pedlar, A., Mundell, C. G. and Geballe, T. R., 1998, MNRAS, 295, 45M
Middelberg, E., Agudo, I., Roy, A. L. & Krichbaum, T. P. 2007, MNRAS, 377, 731
Mills, E. A. C. & Morris, M. R., 2013, ApJ, 772, 105
Moran, J. M., Greenhill, L. J. and Herrnstein, J. R. 1999, JApA, 20, 165
Nishiyama, K., Nakai, N. & Kuno, N. 2001, PASJ, 63, 755
Oka, T., Shimizu, F. O., Shimizu, T. & Watson, J. K. G. 1971, ApJL, 165, 15
Ott, J., Weiss, A., Henkel, C. & Walter, F., 2005, ApJ, 629, 767
Ott, J., Henkel, C., Braatz, J. A. & Weiß, A., 2011, ApJ, 742, 95
Petrov, L. & Taylor, G. B., 2011, AJ, 142, 89

Sawada-Satoh, S., Inoue, M., Shibata, K. M., Kameno, S., Nakai, N. & Migenes, V., 2001, in IAU Symp. 205, Galaxies and their Constituents at the Highest Angular Resolutions, ed. R. T. Schilizzi, 196

Sofue, Y. & Irwin, J. A. 1992, PASJ, 44, 353

Sofue, Y., Koda, J., Kohno, K., Okumura, S. K., Honma, M., Kawamura, A. & Irwin, J. A. 2001, ApJ, 547, L115

Springob, C. M., Masters, K. L., Haynes, M. P., Giovanelli, R. & Marinoni, C. 2009, ApJS, 182, 474

Takano, S, Nakanishi=K, Nakai, N. & Takano, T. 2005, PASJ, 57, L29

Takano, S, Takano, T., Nakai, N., Kawaguchi, K. & Schilke, P. 2013, A&A, 552, 34

Trotter, A. S., Greenhill, L. J., Moran, J. M., Reid, M. J., Irwin, J. A. & Lo, K.-Y. 1998, ApJ, 495, 740

Ulich, B. L. & Haas, R. W. 1976, ApJS, 30, 247

Veilleux, S., Cecil, G., Bland-Hawthorn, J., Tully, R. B., Filippenko, A. V.& Sargent, W. L. W. 1994, ApJ, 433, 48

Walmsley, C. M. & Ungerechts, H. 198, A&A, 122, 16

Walmsley, C. M., Baudry, A., Guilloteau, S., & Winnberg, A., 1986, ApJ, 167, 151

Weiß, A., Neininger, N., Henkel, C., Stutzki, J., & Klein, U. 2001 ApJ, 554L, 143W

Winnberg, A., Walmsley, C. M. & Churchwell, E. 1978, A&A, 66, 431

Yamagishi, M., Kaneda, H., Ishihara, D., Komugi, S., Suzuki, T. & Onaka, T. 2010, PASJ, 62, 1085

Yamauchi, A., Nakai, N., Sato, N. & Diamond, P., 2004, PASJ, 56, 605

Zhang, Q., & Ho, P. T. P., 1995, ApJ, 450L, 63